The solution NMR structure of a blue-green algae hepatotoxin, microcystin-RR
A comparison with the structure of microcystin-LR

Gull-Britt TROGEN[1], Ulf EDLUND[1], Göran LARSSON[2] and Ingmar SETHSON[1]

[1] Department of Organic Chemistry, Umeå University, Umeå, Sweden
[2] Department of Medical Biochemistry and Biophysics, Umeå University, Umeå, Sweden

The microcystin-RR structures are compared with the structures of microcystin-LR in solution as well as in the crystal structure of the complex with protein phosphatase. The gross structures of the two peptides are similar, but with a more accentuated and compact saddle structure for microcystin-RR. The structural differences affect the hydrogen-bond pattern in the peptides and the location of the side chain of *N*-methyldehydroalanine, both of which are important for the ability of the peptide to form a tight complex with protein phosphatase. These structural differences may contribute to the observed differences in toxicity of microcystin-RR and microcystin-LR.

Keywords: microcystins; cyanobacteria; protein phosphatase; three-dimensional structure; simulated annealing.

It is well known that protein phosphatases (PPs) are able to convert glycogen phosphorylase from the active α form to the inactive β form [1]. We know today that reversible protein phosphorylation plays a key role in controlling intracellular events as diverse as the light response in plants and muscle contraction in animals [2, 3]. Phosphatases that act on phosphorylated serine and threonine residues are present in all eukaryotic cell types. It has been found that these enzymes participate in, e.g. carbohydrate and lipid metabolism [4], maintenance of cytoskeletal structure [5], signal transduction and cell growth control [6]. Marked cellular effects can consequently be induced by inhibitors, ranging from collapse of the cytoskeleton to tumor promotion. A number of naturally occurring toxins have been identified as powerful and specific inhibitors of the type-1, -2A, and -2B families of serine/threonine phosphatases [7]. Protein phosphatase 1 (PP-1) and protein phosphatase 2A (PP-2A) are inhibited by the membrane-permeable polyether okadaic acid [8] and by toxic cyclic peptides from fresh, brackish and marine water like microcystins [9, 10] and nodularin/motuporin [11, 12]. The microcystin/nodularin hepatotoxins are produced by cyanobacteria in the genera *Microcystis*, *Anabena*, *Oscillatoria* and *Nodularia* that grow in fresh and brackish water all over the world and thus represent a serious health risk for mammals [13]. Due to a selective uptake system present in liver cells, microcystins and nodularins inhibit PPs in the hepatocytes. Acute microcystin poisoning is characterized by specific liver damage [14].

Correspondence to I. Sethson, Dept. Org. Chem., Umeå University, S-90187 Umeå, Sweden

Fax: +46 90 13 88 85.

E-mail: ingmar@chem.umu.se

Abbreviations. MCLR, microcystin-LR; MCRR, microcystin-RR; 2D, two dimensional; 1D, one dimensional; MD, molecular dynamics; SA, simulated annealing; Mdha, *N*-methyldehydroalanine; Masp, D-*erythro*-β-methylaspartic acid; Adda, (2*S*,3*S*,8*S*,9*S*)-3-amino-9-methoxy-2,6,8-trimethyl-10-phenyldeca-4,6-dienoic acid; Me₂SO, dimethyl sulfoxide; PP, protein phosphatase; TPPI, time-proportional phase incrementation; DQF, double quantum filtered.

Enzyme. Protein phosphatase 1 and 2A (3.1.3.16).

All microcystins (Fig. 1) are characterized as monocyclic heptapeptides containing the β-amino acid (2*S*,3*S*,8*S*,9*S*)-3-amino-9-methoxy-2,6,8-trimethyl-10-phenyldeca-4,6-dienoic acid (Adda). Adda has also been identified as a constituent amino acid of the structurally related pentapeptide toxin nodularin [15, 16]. The main structural difference between various microcystins is the variation of the two L-amino acids labeled X and Z in Fig. 1. Omitted methyl substitutions of D-*erythro*-β-methylaspartic acid (Masp) and *N*-methyldehydroalanine (Mdha) are also common structural modifications [17]. More than 40 different microcystins have so far been isolated and characterized [15].

Several structural NMR studies of the free conformations of microcystins and nodularin/motuporin in different solvents have been published [18−22]. Most of the published three-dimensional (3D) structures of both hepta and penta peptides have basically a saddle-shaped backbone with the Adda side chain protruding behind it. In neat dimethylsulfoxide (Me₂SO), however, the main conformational characteristics of microcystin-LR (MCLR) and microcystin-LY were found to consist of a compact ring with the side chain of Adda pointing upwards from the ring [20]. Recently the 3D X-ray structure of the subunit of PP-1 complexed with MCLR has been determined [23]. Molecular models on microcystin-LR and microcystin-LL, motuporin, ocadaic acid, and calyculin have been docked to the active site of the enzyme using Monte Carlo simulations [19]. Both crystal structure and docking studies reveal that MCLR occupies a cleft near the catalytically active metal ions. The hydrophobic Adda side chain packs in a groove formed by a set of hydrophobic residues. The bound conformation shows close similarity to the conformation of MCLR in solution. This will reduce the entropy loss on binding and can be a factor which contributes to the high affinity of microcystins to PP-1. Moreover, there is a covalent linkage in the complex SS7 between the sulfur atom of Cys273 lin PP-1 and the terminal carbon in Mdha in MCLR, but this bond is not necessary for binding [24]. Several analogues of MCLR and nodularin have been synthesized and tested for interaction with PP-1 and PP-2A [25, 26]. These experiments sup-

Microcystin

Microcystin-LR : R_1 = Leu; R_2 = Arg
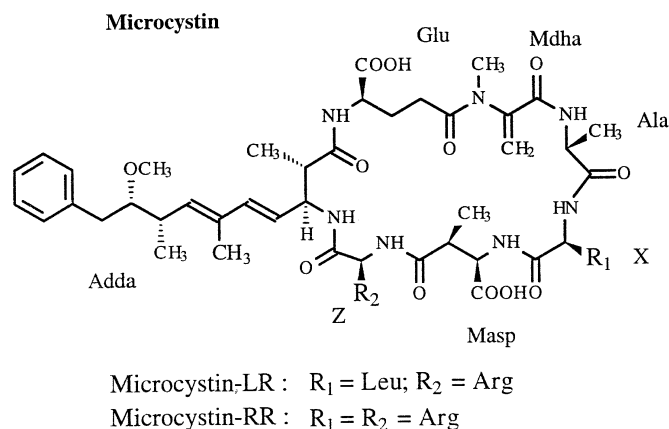
Microcystin-RR : $R_1 = R_2$ = Arg

Fig. 1. Chemical structure of microcystins. R_1 and R_2 are the side chains of the variable L-amino acids.

port the theory that the cyclic system and the Adda residue is essential for the activity.

We recently reported the structures of MCLR in aqueous and dimethyl sulfoxide/water solutions [21] in which data from ¹H-NMR spectroscopy were used. The proton data were subsequently used to obtain three-dimensional structures by molecular dynamics (MD) calculations. Free MD simulations in water were used to investigate the presence of dynamic processes. The results indicate that this peptide essentially adopts a single backbone conformation in both solvents with some structural differences for the residues Mdha7, Ala1 and Leu2. The overall conformation of the molecule was very similar to observed in the X-ray structure of PP-1×MCLR [23] where the structure in the cryoprotective mixture agreed better with the crystal structure. Hence, this solvent was used for the structure determination of microcystin-RR (MCRR), presented in this work. In the present study, the previously determinded structures of MCLR are compared with structures of MCRR, which is ten times less toxic (LD_{50} = 600 µg/kg mice) than MCLR (LD_{50} = 50 µg/kg mice) [15].

MATERIALS AND METHODS

Sample preparation. Lyophilized MCRR from *Microcystis aeruginosa* was purchased from Calbiochem-Novabiochem Corporation. For the NMR measurements, 2–2.5 mg freeze-dried microcystin was dissolved in 0.56 ml Me₂SO and 0.14 ml 20 mM sodium phosphate giving a pH value of 5.9. A Me₂SO-d₆/H₂O (80:20, by vol.) cryoprotective mixture was chosen as a solvent in order to mimic the viscosity in cells [27]. Since receptors for peptides are composed of both hydrophilic and lipophilic portions, such a cryoprotective mixture has the potential to better mimic these properties than aqueous solutions [28]. This assumption may not be generally valid but at least in this case it is supported by the observation that the conformation of MCLR obtained from MD calculations in this medium more closely resembled the structure of the peptide bound to PP-1 as compared to the water solution structure [21].

NMR spectroscopy. The NMR spectra used for assignments and extraction of parameters for MD calculations were conducted at 4 °C. At this temperature the molecular tumbling is in a region of slow motion $[(\omega\tau_c)^2 \gg 1]$. The Me₂SO signal at 2.50 ppm was used as a reference for ¹H in all spectra. The double quantum filtered COSY (DQF-COSY) [29] and TOCSY [30] spectra were recorded on a Bruker AMX2 500 in a phase-sensitive mode via time-proportional phase incrementation

(TPPI) in t_1 [31, 32]. The NOESY [33] spectrum was aquired at 600 MHz on a Varian Unity 600 using the states-TPPI method [34] for frequency sign discrimination in the indirect dimension. The water resonance was suppressed by low-power presaturation ($\gamma\beta_1 \approx 100$ Hz) during the relaxation delay, 1.6–2 s. A SCUBA preparation sequence [35] was used in the DQF-COSY and TOCSY experiment to allow the observation of cross peaks from signals close to the water frequency. The two-dimensional (2D) data for the DQF-COSY and the NOESY spectra were zero-filled and transformed to 4K×2K data matrices, whereas the final processed data matrix for the TOCSY spectrum consisted of 2K×2K data points. The spectral parameters used in the 2D homonuclear experiments are compiled in Table 1.

Proton relaxation times, t_1 (delays = 100, 150, 200, 300, 400, 600 ms, 1, 1.5, 2.5 and 4.0 s) and t_2 (delays: 2.8, 5.6, 8.4, 11.2, 14.0, 19.6 28.0, 42.0, 70.0, and 140.0 ms), were measured using inversion-recovery and CPMG pulse sequences, respectively.

Temperature gradients were obtained from 1D spectra acquired between 5 °C and 35 °C (16 K in size, SW = 7000 Hz, zero-filled to 32 K).

The natural abundance 2D heteronuclear ¹H-¹³C and ¹H-¹⁵N HSQC gradient enhanced spectra were recorded [36] for both MCRR and MCLR. In the ¹H-¹³C experiments, the delays were chosen to enable observation of all carbon multiplicities. The chemical shifts were referenced by using Me₂SO (2.50 ppm for ¹H, and 40.7 ppm for ¹³C, respectively), and indirectly referencing in the ¹⁵N dimension using the frequency ratio (Ξ) ¹⁵N/¹H = 0.101329118 [37]. The spectral parameters used in the heteronuclear experiments are given in Table 1.

Derivation of distance restraints. Internuclear proton-proton distances were generated from the 2D NOE cross peak integrals using the program MARDIGRAS [38, 39]. This program takes spin-diffusion into account as it uses a complete relaxation matrix to extract cross relaxation values. The rotational correlation time, τ_c, used in the MARDIGRAS calculations, was estimated to 2 ns from the relation between the experimental spin-lattice (t_1) and the spin-spin relaxation time (t_2) [40]. Unrestrained MD calculations at elevated temperatures were used to create sufficiently divergent microcystin structures as a representation of the conformational space. Ten structures generated in this way were used in the MARDIGRAS calculations. The extreme values were used as upper and lower bounds for the distance restraints in the structure calculations.

Determination of dihedral angle restraints. Proton-coupling constants were extracted from the DQF-COSY spectrum. In order to obtain coupling constants from cross peaks with complex splitting patterns, the DQF-COSY spectrum was simulated using the programs SPHINX (simulation of pulse sequences in high-resolution NMR experiments) and LINSHA (line shape program) [41, 42]. Dihedral angle constraints were calculated from the coupling constants according to the Karplus relationship [43], using

$$^3J(\text{Hz}) = A\cos^2\theta + B\cos\theta + C , \qquad (1)$$

with the coefficients A = 9.4, B = −1.1, and C = 0.4 Hz for $^3J_{HN, H\alpha}$, and A = 9.4, B = −1.4, and C = 1.6 Hz for $^3J_{H\alpha, H\beta}$.

Structure calculations. To translate the interproton distances and dihedral angles into a three-dimensional molecular structure, restrained MD calculations in vacuo were performed by using the standard protocol for simulated annealing (SA) and SA refinement, as described in the X-PLOR manual, version 3.0 [44]. The three mutually most dissimilar structures (pairwise rmsd >0.2 nm) among the starting structures for the MARDIGRAS calculations were chosen as starting templates for the SA simulations. Distance restraints were incorporated with a soft

Table 1. Parameters for 2D homonuclear experiments. The relaxation delay was 1 s in all experiments. TD, time domain points; SF, spectral frequency; SW, spectral window.

Experiment	Mixing time	SF (^{1}H)	NS	TD		SW	
				t_1	t_2	t_1	t_2
	ms	MHz		points		Hz	
NOESY	200	600	32	1024	2048	10 000	7000
DQF-COSY		500	128	750	2048	8 333	5000
TOCSY	75	500	32	512	2048	8 013	8002

Peptide	Nucleic	SF (^{1}H)	NS	TD		SW	
				t_1	t_2	t_1	t_2
		MHz		points		Hz	
MCRR	^{1}H-^{15}N[a]	600	1000	206	1024	4 167	7142
MCRR	^{1}H-^{13}C[b]	500	160	670	1024	25 000	8333
MCLR	^{1}H-^{15}N[a]	600	1000	94	1024	4 167	7142
MCLR	^{1}H-^{13}C[a]	600	100	720	1024	25 000	8333

[a] Conducted at 30°C.

[b] Conducted both at 4°C and 30°C.

square-well potential and dihedral angle restraints with a square-well potential in the protocol, with force constants of 209 kJ · mol^{-1} · Å^{-2} and 837 kJ · mol^{-1} · rad^{-2} for distance and dihedral angles, respectively. For the SA refinement, a square-well potential was used for both types of constraints.

A total number of 300 structures was calculated, 100 from each of the three templates. After minimization, the protocol performed a 30-ps restrained molecular simulation at 1000 K. In the next stage, the system. was cooled down to 100 K within 15 ps. In the subsequent refined SA calculations, the system was initially heated to 1000 K, then slowly cooled to 100 K during 21 ps. The integration step of the equations of motion was set to three fs in all calculations. All SA calculations were followed by 300 steps of Powell's energy minimization. No hydrogen-bond constraints were used in the calculations. For comparison, 300 structures were also calculated without dihedral constraints.

The stability of the structure (with the lowest violation of distance constraints) was confirmed by an MD simulation with explicit inclusion of water molecules using the program CHARMm [45]. The structure of MCRR was immersed in a rectangular box with the dimensions 3.41×2.79×2.79 nm³ containing 863 water molecules. All water molecules closer than 0.28 nm to the solute peptide molecule were removed. The system consisted of 2540 atoms after the removal of these overlapping molecules. The peptide and the water molecules were subjected to free MD calculations with periodic boundary conditions. All atoms were given initial velocities from a Maxwellian distribution at 98 K. The system was heated to 298 K during the first picosecond and, after every 100 steps, the velocities were reassigned. If the temperature of the system deviated more than ±10 K, the reassignment of the velocities was continued during the second picosecond. Using the same criterion during the next 20 ps, the velocities were rescaled. The simulation was performed up to 1 ns without any external perturbations after these 22 ps. The integration of equations of motion was carried out using 1-fs steps.

Analysis of solution structures. To describe the quality of a well-ordered solution structure determined by NMR, rmsd values between pairs of structures in an ensemble (precision), and

R factors describing the fit between calculated and experimental NOE intensities (accuracy), were used [46, 47]. Superpositions and rmsd calculations were performed for all backbone atoms (N, C$^\alpha$, and C for residues 1 through 7, and C$^\beta$ for residues 3, 5, and 6, and C$^\gamma$ for residue 6) if not otherwise stated.

The residual index or the R factor [47]

$$R = \sum (|I_o| - |I_c|)/\sum i_o$$

and a modified R factor [48]

$$R_1^x = \sum (I_o^{1/6} - I_c^{1/6})/\sum I_o^{1/6},$$

where I_o and I_c are the intensities of observed and calculated NOE cross peaks, were calculated with the program CORMA [38].

RESULTS

Resonance assignments. The proton resonances were assigned by using standard sequential assignment procedures [49]. The chemical shifts of the non-exchanging protons are in good agreement with previous published assignments in D$_2$O [50].

Selection and quantification of NOE restraints. A total of 93 NOEs were assigned from the NOESY spectrum. The cross peaks were converted to distance restraints resulting in 73 accepted distance restraints for the structure calculations. The restraints consisted of 48 intra-residue, 18 sequential and 7 medium range [4($i,i+2$) and 3($i,i+3$)] connectivities. The distribution of the observed NOE connectivities is shown in Fig. 2.

Coupling constants and dihedral angle restraints. Vicinal $^3J_{HN, H\alpha}$ coupling constants were determined from a DQF-COSY spectrum processed to give a high digital resolution. The observed $^3J_{HN, H\alpha}$ constants were corrected for electronegativity effect of the C$^\alpha$ substituents using the relation $^3J_{HN, H\alpha} = 1.09 \times J_{obs}$ [43]. All the measured coupling constants for the amide protons were larger than 8.0 Hz (Table 2) which to some extent indicate structural rigidity [51] in the cyclic backbone of MCRR. The
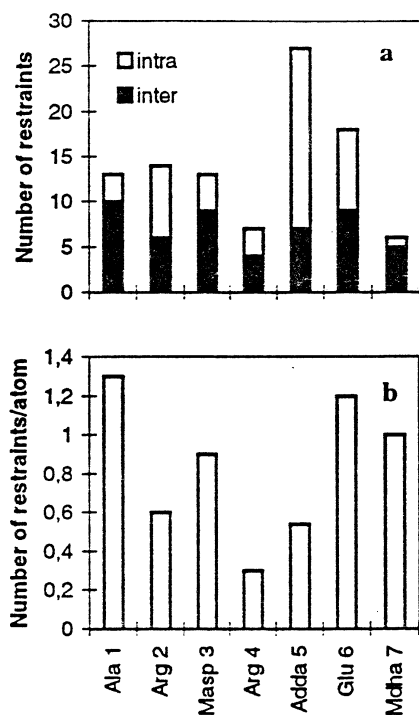
Fig. 2. Distribution of the observed NOE connectivities in microcystin-RR. Per residue (a), and per residue and atom (b).

Table 2. Some observed and calculated coupling constants for microcystin-LR and microcystin-RR.

Residue	Atoms	Coupling constant			
		observed		calculated	
		MCLR	MCRR	family A	family B
		Hz			
Ala1	N^N-H^α	7.5 ∓ 1	9 ∓ 1	7.5	5.7
Arg2 Leu2	H^N-H^α	7.6 ∓ 0.5	9 ∓ 0.5	7.8	9.8
	H^α-$H^{\beta 1}$	–	6 ∓ 0.5	2.8	3.9
	H^α-$H^{\beta 2}$	–	8 ∓ 1	10.8	11.4
	$H^{\beta 1}$-$H^{\gamma 1}$	–	10 ∓ 1	11.3	11.3
	$H^{\beta 1}$-$H^{\gamma 2}$	–	5 ∓ 1	2.7	2.7
	$H^{\beta 2}$-$H^{\gamma 1}$	–	4.5 ∓ 0.5	4.8	4.8
	$H^{\beta 2}$-$H^{\gamma 2}$	–	12 ∓ 1	11.4	11.4
Masp3	H^N-H^α	10.9 ∓ 0.5	11 ∓ 1	9.6	9.6
Arg4	H^N-H^α	12.0 ∓ 0.5	12 ∓ 1	10.4	10.5
	H^α-$H^{\beta 2}$	–	9 ∓ 1	6.1	6.0
Adda5	H^N-H^β	8.7 ∓ 1	9 ∓ 1.5	10.5	10.1
	H^β-H^4	9 ∓ 0.3	8 ∓ 1.5	11.9	11.6
Glu6	H^N-H^α	9.8 ∓ 0.5	11 ∓ 1	9.4	10.5
	H^α-$H^{\beta 1}$	9 ∓ 1	6.5 ∓ 1	4.0	2.1
	H^α-$H^{\beta 2}$	9 ∓ 1	11 ∓ 1	5.9	11.8
	$H^{\beta 1}$-$H^{\gamma 1}$	12 ∓ 1	5 ∓ 1	2.8	3.1
	$H^{\beta 1}$-$H^{\gamma 2}$	3 ∓ 1	9 ∓ 1	12.2	12.4
	$H^{\beta 2}$-$H^{\gamma 1}$	4 ∓ 1	9.5 ∓ 1	12.3	12.4
	$H^{\beta 2}$-$H^{\gamma 2}$	12 ∓ 1	5 ∓ 1	3.8	3.4

same COSY spectrum was used to extract coupling constants between α and β protons and between β and γ protons for characterization of the χ^i angles (Table 2). In some cases, the direct coupling between two protons could not be determined due to spectral overlap.

Table 3. Comparison of the temperature dependence of the chemical shifts, given as $-\varDelta\delta/\varDelta T$, between microcystin-RR and microcystin-LR.

Peptide	$-\varDelta\delta/\varDelta T$					
	Ala1	Arg/ Leu2	Masp3	Arg4	Adda5	Glu6
MCRR	8.7	$-$[a]	0.0	5.3	0.0	0.0
MCLR	11.6	6.0	0.0	7.2	0.7	2.6

[a] -3.5 ppb/K in the range $278-293$ K, and -1 ppb/K in the range $293-308$ K.

However, some of these coupling constants could be determined from an estimation of passive couplings in cross peaks to other *J*-coupled protons in the same spin system. This approach did not give a coupling constant as accurate as when applied on direct couplings, but accurate enough to determine if preferred conformations are present.

Amide proton temperature dependence. The temperature dependence of the backbone amide proton chemical shifts were used to confirm if any of the amide protons were involved in hydrogen bonding and/or shielded from the surrounding aqueous environment [52]. All amide proton resonances were shifted upfield by increasing temperatures. The temperature coefficients for the amide protons of Ala1 and Arg4 indicate that they are accessible to the solvent (Table 3). The amide protons of Arg2, Masp3 Adda5 and Glu6 had negligible temperature coefficients, indicating the existence of intramolecular hydrogen bonding or steric shielding of the protons from the solvent. The chemical shifts varied linearly with the temperature except for Arg2. The change in solvent accessibility for the amide proton in this amino acid may be an indication of a different conformation at temperatures above 25 °C. The temperature coefficient in the range $4-25$ °C for Arg2 is -3.5 ppb/K. The corresponding value between $25-35$ °C is -1.0 ppb/K.

Solution structures using standard restraints. As MCRR is a cyclic peptide and contains unusual amino acids, it is not obvious that the ϕ dihedral angles are negative in L-amino acids, and positive in D-amino acids [53]. In order to obtain information about the ranges of ϕ angle constraints, 300 structures were calculated using a SA protocol followed by refined SA calculations *in vacuo* using only distance restraints. Of the 300 calculated structures, 269 were accepted using the criteria for acceptance discussed above. Using these structures and the angles derived from the observed coupling constants, the range for the dihedral constraints was chosen.
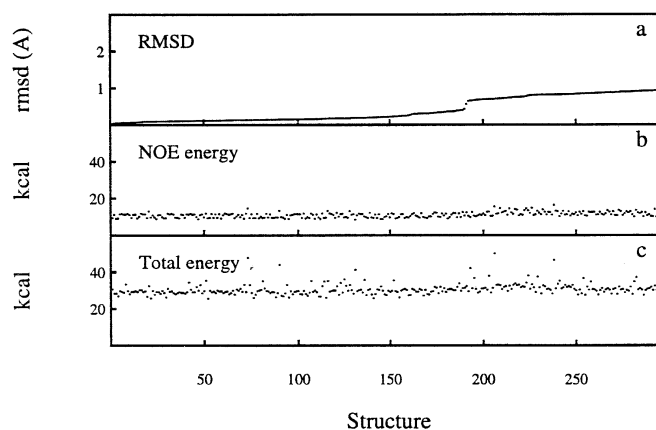
In a calculation where the dihedral constraints were included, 297 out of 300 structures were accepted. The quality of the accepted structures was analyzed using *R* factors, constraint violations, and rms deviations. The rmsds to the mean structure of all backbone atoms were 37 pm and of all heavy atoms 180 pm (Table 4). These values are larger compared with the corresponding values for MCLR obtained in a previous study [21]. When all structures were inspected, it was noticed that the 297 accepted structures could be divided into two main families with 191 structures in family A and 106 in family B. The X-PLOR conformational energy (average total energy = 125.4 ∓ 7.7 kJ · mol^{-1}) could not distinguish the two families (Fig. 3). rmsd data for each family are compiled in Table 4 and it is evident that the cyclic backbone is very well defined within each ensemble according to structural statistics in Table 4. The

Table 4. Summary of input restraints for the restrained MD calculations and structural statistics of the final structures.

	MD with standard restrain	MD without dihedral constrain
Input to structure calculations		
Interproton distance restraints		
total	73	73
intraresidue	48	48
sequential	18	18
medium range	7	7
Dihedral angle restraints		
ϕ	6	–
χ	2	–
Total restraint/residue	11.6	10.4
Results of structure calculations		
Energy (kcal · mol^{-1})		
total	125.39 ± 7.70	117.32
bonds	24.18 ± 4.64	18.92
angles	48.45 ± 7.53	50.08
impropers	2.52 ± 3.18	3.60
vdw	3.81 ± 1.89	4.18
NOE restraints	46.07 ± 5.44	40.54
Dihedral restraints	0.33 ± 0.29	–
NOE violations		
number > 10 pm	7.30	5.42
number > 20 pm	0.10	0.22
number > 30 pm	0	0
The fit of theoretical and experimental NOE		
R (intra)	0.300	0.277
R (inter)	0.138	0.141
R (tot)	0.234	0.221
R_1^x (intra)	0.056	0.053
R_1^x (inter)	0.041	0.037
R_1^x (tot)	0.050	0.047
Pairwise RMSD (pm)		
BB heavy atoms	50 ± 30	60 ± 22
all heavy atoms	252 ± 64	279 ± 61
RMSD from mean structure (pm)		
BB heavy atoms		
all structures	37	–
family A	19	–
family B	23	–
All heavy atoms		
all structures	180	–
family A	172	–
family B	175	–

Fig. 3. rmsd and energy distribution for the SA structures. The structures from 1 up to 191 constitute family A in all the three panels. The remaining structures form family B. Panel a shows the rmsd for the accepted structures after restrained SA calculations. The structure with the lowest total energy is used as reference. Corresponding NOE energies and total conformational energies for each structure are displayed in (b) and (c), respectively.

R and R_1^x factors calculated with the program CORMA show good overall fit between theoretical and experimental NOEs (Table 4). The residual indices R_1^x are slightly smaller for the structures calculated without dihedral constraints indicating some discrepancy between NOEs and coupling constants.

The two solution structures of MCRR are shown in Fig. 4 where superpositions of 20 structures, randomly chosen from each family, are displayed. The peptide ring is saddle-shaped in both ensembles with the Adda side chain directed away from the cyclic backbone and well-defined in close proximity to the ring. The side chains of the two arginine residues also point

away from the ring. The negatively charged carboxyl groups of Masp and Glu are located below the saddle. The average structures are superimposed and aligned to each other using backbone heavy atoms from Arg2 through Adda5. The rmsd for backbone heavy atoms in this part is 20 pm, compared with 114 pm for all the heavy backbone atoms. Backbone conformational differences between the two families are predominantly found in Glu6 and Mdha7. Family A has ψ dihedral angles in the range 95° to 148° for Glu6 and ϕ dihedral angles in the range −73° to −36° for Mdha7, whereas family B has ψ dihedral angles clustered around 63−78° for Glu6 and ϕ dihedral angles clustered around 10°−61° for Mdha7 (Figs 4 and 5).

A number of hydrogen bonds were found using the hydrogen-acceptor distance criterion ≤0.30 nm and the donor-hydrogen-acceptor angle criterion in the range 120°−180°. In almost all structures (family A + family B), hydrogen bonds between Glu6H^N and the oxygens of COO$^-$ in Masp3, and between Adda5H^N and the Masp3-COO$^-$ group were observed. Backbone to backbone hydrogen bonds across the macrocyclic ring, from amide protons in Arg2 and Masp3 to the carbonyl oxygen in Glu6, were identified only in family B.

Results from free MD simulation and comparison with restrained MD calculation. In order to gain more insight into dynamic processes of MCRR in solution, unrestrained molecular dynamics calculations of MCRR with explicitly included water molecules were performed up to 1 ns. Two calculations were performed in which the structure with lowest total energy from each family obtained from the SA calculations was used as starting structure. Both the temperature profiles and the rmsd of the backbone atoms during the calculations indicate that the initial structures did not drift away from their starting positions. However, as indicated by the distance Masp3H^N−Ala1H$^\alpha$, the conformations sampled during the first 200 ps with family A as the starting structure, did not reappear later on during the MD simulation. Some of the distances and torsion angles in the backbone showed significant fluctuations occurring in the nano-second to pico-second timescale throughout the simulation.

The torsion angles ϕ in Arg4, Adda5 and Mdha7, and ψ in Arg4 and Glu6 changed between the values observed for the different families in the SA calculations. Some of the interproton
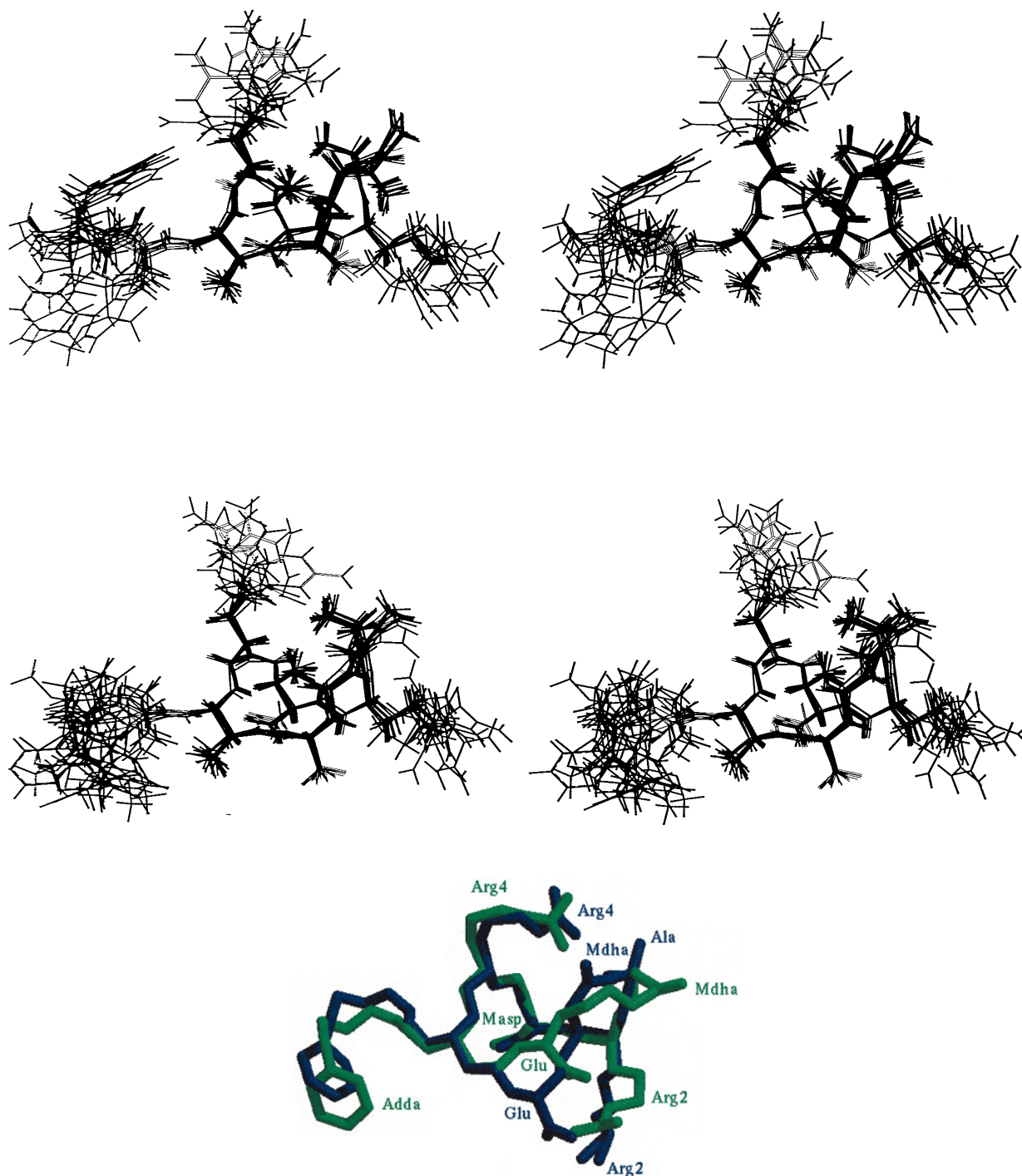
Fig. 4. Superimpositions of ten randomly chosen structures of microcystin-RR. Family A in (A), family B in (B) and superimposition of the average structures (backbone atoms) from each family is shown in (C), where the average structure of family A is illustrated green. The rmsd of the backbone atoms superimposed on each other from residue 2 up to 5 is 20 pm.

distances also differed between the various conformations sampled during the unrestrained MD. These distances were compared with their experimentally derived counterparts, if present, and five were found to deviate more than 50 pm from the upper/lower bound of the experimental distance restraints. Two of those, Adda5H^N−Adda5H^4 and Adda5H$^\beta$−Adda5H^5, which are responsible for the alignment of the Adda side chain with respect to the cyclic backbone of MCRR, show fluctuations upon rotation around the C$^\beta$-C^4 bond, observed in the unrestrained MD calculation (Fig. 6a). The Adda5H^N−Adda5H^4 distance is close to 0.3 nm and 0.5 nm for the two different conformations, re-

spectively, as compared with the experimentally estimated distance of < 0.3 nm. The conformation with the shorter distance has a dihedral angle corresponding to a coupling constant of 12 Hz, vs. $^3J_{H\beta, H4} = 4$ Hz in the other conformation. The experimentally determined coupling constant is 8 ± 1.5 Hz.

The experimentally determined distance between Masp3H^N−Glu6H$^{\beta 2}$ has an upper bound of 0.33 nm. The observed distance in the unrestrained MD calculations varies between 0.3−0.6 nm, where 52% of the structures have a distance shorter than 0.33 nm. The calculated $^3J_{H\alpha, H\beta 1}$ coupling constant for Glu6 in conformations having a long distance between
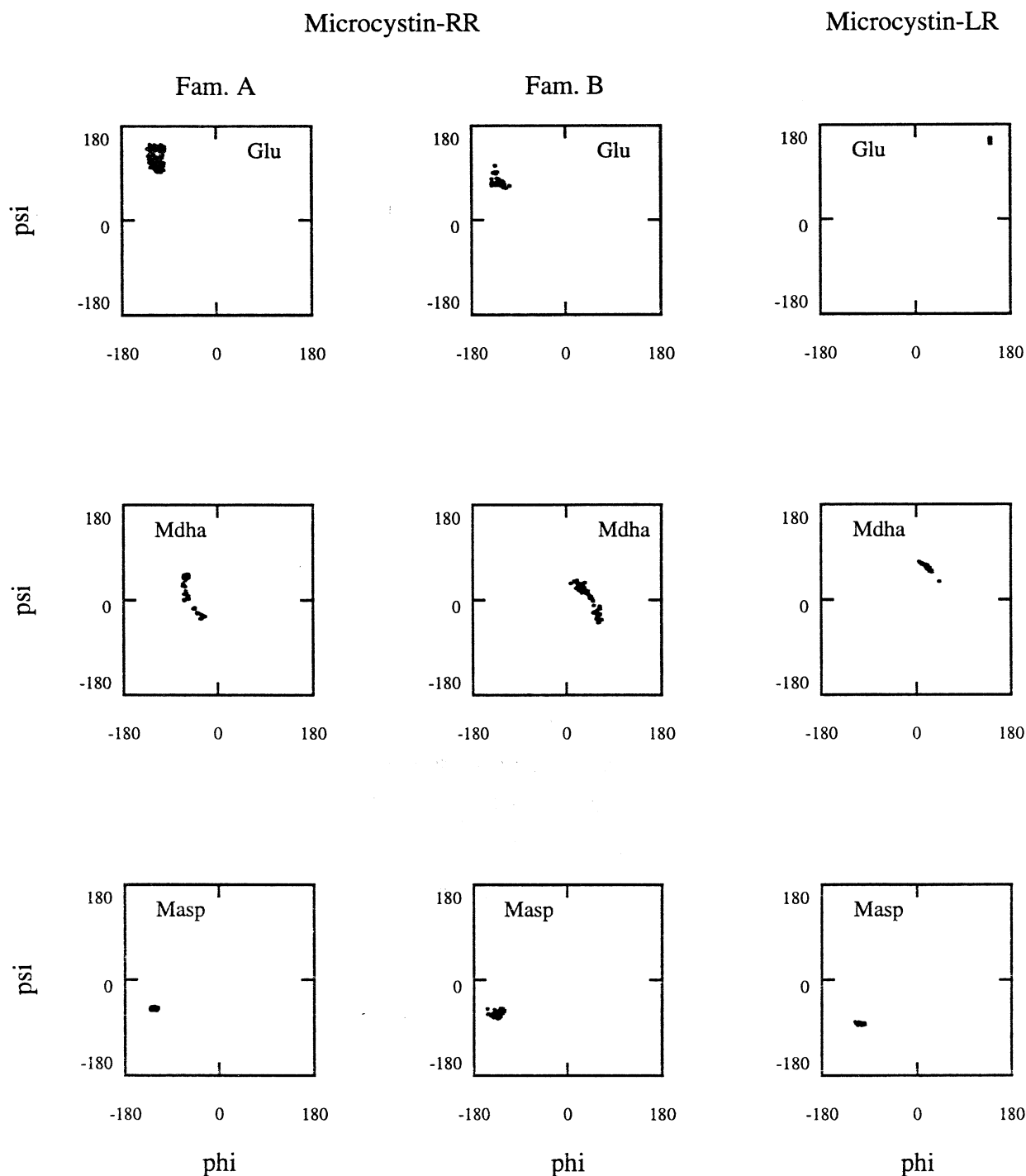
Fig. 5. Ramachandran plots for the three residues in microcystin-RR and -LR with the largest conformational differences. The distribution of the conformations for Mdha can be interconverted by inversion at the center of the Ramachandran plot since Mdha is achiral.

$Masp3H^N - Glu6H^{\beta2}$ is small (3–5 Hz). The experimentally observed coupling constant is 11 Hz, which is close to the value calculated from the structures with short distances.

DISCUSSION

Relating NMR parameters to calculated structures. The two families of MCRR observed in the SA calculations differ mainly due to variations of dihedral angles in the amino acids Glu6 and Mdha7 (Fig. 5). The structures found in family B are charac-

terized by a more pronounced and compact saddle structure, in comparison with family A (Fig. 4C). The different location and direction of the carboxyl group of Glu6 is one striking feature. The structure of B allows the carbonyl group of this amino acid to form a hydrogen bond with the amide proton of Arg2. This is compatible with the low observed temperature coefficient for the amide proton chemical shift of Arg2 in MCRR, suggesting that family B may be the best representative of the average structure of MCRR. However, the two families A and B are presumably involved in a rapid exchange since the observed coupling constants for χ^1 and χ^2 in the cyclic backbone for Glu6
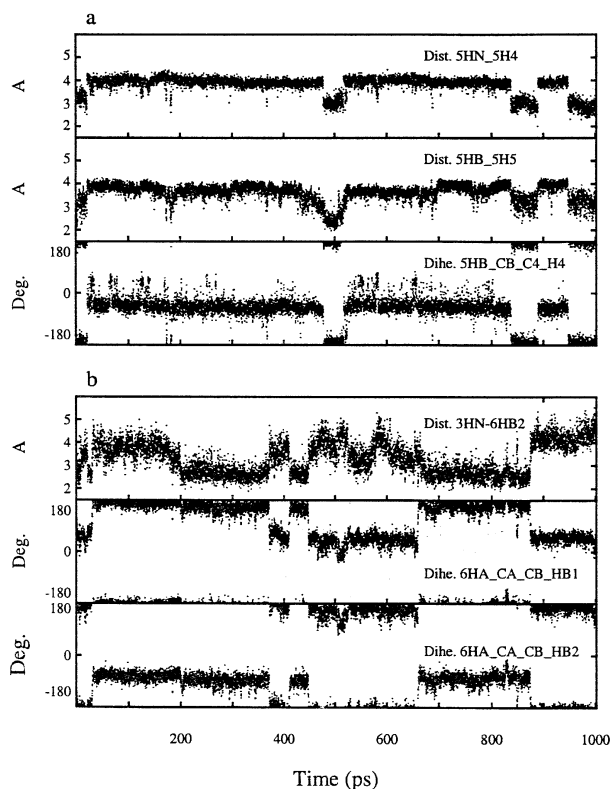
Fig. 6. Evolution of some distances and dihedral angles from the unrestrained MD simulation in water. Data are shown from 10 020 coordinate data sets, sampled every 100 fs. (a) Two distances and one dihedral angle in Adda5 are shown to visualize the mobility of this side chain. (b) The evolution of two dihedral angles in Glu6 and one distance across the ring from Masp3H^N to Glu6H$^{\beta2}$.

are in the boarder region between a preferred conformation and equilibrating conformers.

Structural studies of small peptides are normally met by difficulties due to the presence of conformational averaging. However, it is known that cyclic peptides tend to be more structured than linear ones. Besides, the experimentally obtained NMR parameters are an average of all conformers present in solution. It is therefore important to examine available NMR data with caution, due to the inverse sixth power dependence of the NOES. The distances determined from NOEs may be biased toward short distances emanating from conformations only transiently present in solution.

Consequently, it is important to include other NMR parameters, which are truly weighted according to the thermodynamic distribution of conformations present in solution. Coupling constants, which provide information about torsion angles have this property. The appearance of the two families in the SA calculations is due to the fact that the conformational exchange provides NOEs that are incapable to sample all the existing conformations. In fact, the fit between calculated and experimental NOE intensities (the *R* factors) is better when all 296 structures are treated as one ensemble in comparison with each family ($R_{296} = 0.234$, $R_A = 0.248$, $R_B = 0.245$).

Calculations, with and without the dihedral constraints, were performed in order to investigate if the experimentally determined distance and torsion angle restraints are compatible with each other. The generated structures differed only slightly whether the dihedral constraints were included or not. When the back-calculated spectra were compared with the experimental NOESY spectrum, the *R* value was 0.277 when the *J* couplings

were excluded, and 0.300 when they were included. These results indicate that the measured NOEs grossly correspond to distances observed in one major conformation, although there are some discrepancies (Table 4).

The observed coupling constants in the 'side chain' of Glu6 ($^3J_{H\alpha, H\beta1} = 6.5 \pm 1$ Hz and $^3J_{H\alpha, H\beta1} = 11 \pm 1$ Hz) suggest averaging between conformers and they were therefore not used in the SA calculations to constrain the dihedral angles. Unrestrained MD provides further support for the existence of such a conformational exchange. During the time course of the unrestrained MD, Glu6 frequently changes conformation and the dwell times for these conformations are roughly equal. Furthermore, the observed fluctuations are time-correlated with the fluctuations in the interproton distances Masp3H^N−Glu6H$^{\beta2}$ and Arg4H^N−Ala1H$^\alpha$, which vary strongly during the unrestrained MD. Hence, it is reasonable to suspect that the SA-calculated structures may be biased towards conformations where these interproton distances are short. The conformations in the unrestrained MD, where the Masp3H^N−Glu6H$^{\beta2}$ distance is ≈0.5 nm have dihedral angles giving back-calculated coupling constants close to 5 Hz for $^3J_{H\alpha, H\beta1}$ (Fig. 6b), whereas the conformations having distances ≈0.3 nm afford back-calculated coupling constants of about 10 Hz. The corresponding back-calculated values for $^3J_{H\alpha, H\beta2}$ are 11 Hz and 3 Hz, respectively. The NMR data indicate that the conformation with smaller inter-proton distances is much less populated since structures where the Masp3H^N−Glu6H$^{\beta2}$ distance is large (≈0.5 nm) give back-calculated coupling constants closer to the observed ones. With such an assumption of the difference in relative populations, the observed NMR parameters are compatible with the conformations observed in the unrestrained MD calculations. If this is correct, the result of the SA calculations will not accurately describe the conformations present for this amino acid, since short distances will be overemphasized. The structures in family A give back-calculated coupling constants corresponding to *gauche* in χ^1 and family B consists of structures with *trans* conformation. It is impossible to fit any of the back-calculated values to the actually observed coupling constants, whether or not an exchange between these two conformations is taken into account. Accordingly, the NMR data rather indicate that the two SA families are poor representatives of the actual exchanging conformers.

Another question that should be addressed is whether the compact saddle-shaped structure of MCRR could result from NOEs observed from sparsely populated conformations where the Masp3H^N−Glu6H$^{\beta2}$ and Arg4H^N−Ala1H$^\alpha$ distances are short. To check this, SA calculations were performed without these distance constraints.

However, no structure having distances outside the ranges allowed by these constraints was found. This demonstrates that neither of these two constraints define the compact saddle-structure of MCRR in the SA calculations. Since no other interproton distance in the unrestrained MD fluctuates outside the ranges of the used constraints, the obtained structure of the macrocyclic ring is indeed a valid model for the various conformations present.

The observed $^3J_{H\beta, H4} = 8 \pm 1.5$ Hz in the Adda side chain indicates that the dihedral angle may not be well-defined. In the unrestrained MD the corresponding torsion angle fluctuates between conformations that would give rise to coupling constants of 4 Hz and 12 Hz, respectively (Fig. 6a). Unfortunately, the strong NOEs that are measured can be a net result of a transiently populated conformation, provided the corresponding distances are short. Consequently, the SA calculations, which are based only on NOE constraints for the Adda side chain, may be misleading. The so far reported NMR structures of microcystins and nodularin have as a common feature that the orientation

of the Adda side chain is well defined in the proximity of the macrocyclic ring [18−22]. Both our present findings and our previous study of MCLR indicate that the well-defined structures of Adda may be an artifact caused by an overestimation of short distances by the NOE measurements. Accordingly, we suggest that the unrestrained MD calculations constitute a better model for the structure of the Adda side chain in solution. The side chain of Arg2 also appears to be artificially too well-defined in the SA structures. The SA calculations, which are based solely on NOEs for this side chain, generated mainly *trans* structures, i.e. where $^3J_{H\alpha, H\beta2} - {}^3J_{H\alpha, H\beta1} > 5$ Hz [54]. This conformation is not compatible with the measured coupling constants $^3J_{H\alpha, H\beta1} = 6$ Hz and $^3J_{H\alpha, H\beta2} = 8$ Hz, which rather indicate averaging between *gauche* and *trans* conformers.

The presence of hydrogen bonds slows down the amide proton exchange with solvent resulting in low observed amide proton temperature coefficients in peptides. This is consistent with the observation that the hydrogen bonds identified in the calculated structures of MCRR do have small amide proton temperature coefficients. Hydrogen bonding between Glu6H^N and Masp3-O$^{\delta1}$, and Adda5-H^N and Masp3-O$^{\delta1}$ in both families are reflected in the negligible amide proton temperature coefficients. In family B, 97% of the structures have hydrogen bonds between Glu6 C=O and Arg2H^N and Masp3H^N, respectively. The mean values of the corresponding distances in family A are > 0.4 nm. The temperature coefficients of Arg2 and Masp3 are also small, which support the presence of these hydrogen bonds. This would suggest that family B is a better representative of the conformational ensemble, although it cannot be excluded that steric hindrance effects also contribute to the temperature coefficients. Another indication of the conformational flexibility is the observed change in the temperature coefficient for Arg2 at higher temperatures. Such a change is presumably a result of changes in the relative populations of the various conformers.

Comparison with previous conformational studies of MCLR. Recently we reported the 3D structure of MCLR using NMR spectroscopy in aqueous and cryoprotective solutions [21]. The conformations of MCLR were investigated by using the same methodology as for the conformational analysis of MCRR used in this study, i.e. SA calculations and unrestrained MD calculations. The structures observed in both solvents revealed the same overall shape of the cyclic structure, although some distinct differences were apparent. The macromolecular ring was saddle shaped in both solvents with the carboxyl groups in Masp and Glu positioned below the saddle. The side chains of Arg4 and the remote part of Adda5 did not show any well-defined structure. The largest differences between the two structures were found in the region that contains the residues Mdha7, Ala1 and Leu2. As a result, the β carbon of Mdha in the minimized average water structure pointed upwards from the saddle, whilst this atom pointed downwards in the structure determined in the cryoprotective solution. The latter conformation is also observed in the crystal structure, which allows the β carbon of this residue to form a covalent bond between Cys273 of PP-1.

The minimized average structures from both families of MCRR were compared with the minimized average structure of MCLR in the cryoprotective solvent. The rmsd's of all backbone atoms were 77 pm (family A) and 159 pm (family B). When the backbone segment consisting of the residues from Arg2/Leu2 up to Adda5 was superimposed onto the corresponding part of free MCLR, the rmsds between the two structures were reduced to 37 pm in family A and 44 pm in family B for these residues, confirming the similarities for the backbone atoms in this region. The saddle-shaped structure of MCLR can also be observed in both families of MCRR. Strong cross-peaks can be seen between

the N-methyl group in Mdha7 and H$^\gamma$s of Glu6 in the NOESY spectrum indicating a *trans* peptide bond as in MCLR. The Adda side chain is constrained in the vicinity of the backbone in both peptides in the SA calculated structures, but measured coupling constants and unrestrained MD suggest equilibrating conformers. The side chain of Arg4 appears to lack any well-defined structure in both peptides. The observed degenerate chemical shifts of the H$^\gamma$s support this observation. The broad linewidth of the guanidinium resonances of Arg4 in MCRR, as compared to Arg2, is another indication of a less defined structure. The observed non degenerate resonances of the aliphatic protons suggest that Arg2 is more structured. The differences between the structures of MCLR and MCRR are mainly located in amino acids Glu6, Mdha7 and Ala1. The conformational differences are illustrated in the form of Ramachandran plots (Fig. 5) and superimposed structures (Fig. 7A). A number of NOEs across the cyclic ring in MCRR (Glu6H^N−Masp3H$^\alpha$; Masp3H^N−Glu6H$^{\beta2}$; Ala1H^N−Arg4H$^\alpha$) results in a more compact and pronounced saddle structure as compared with MCLR. In contrast to MCLR, this structural feature of MCRR allows the amide group of Glu6 to form a hydrogen bond with the carboxyl group in the side chain of Masp3. Another observable difference is that the side chain of Mdha in MCRR, as opposed to MCLR, points upwards (Fig. 4C). This conformation has to be changed in order to enable the formation of the covalent bond between the peptide and the protein observed in the crystal structure of the MCLR-PP1 complex.

The inspection of the chemical shifts of the backbone atoms as well as the temperature dependence of the chemical shifts of the amide protons provide additional evidence for the observed structural differences between MCLR and MCRR. It is known that the torsion angles ϕ and ψ [55] are the most important contributors to the ^{13}C chemical shift differences ($\Delta\delta^{13}$C) observed between 'random coil' amino acids, as compared to amino acids located in regular secondary structures. Consequently, a significant change in $\Delta\delta^{13}$C for amino acids having the same sequential neighbors would reflect changes in conformation. The $\Delta\delta^{13}$C values in Glu6 (-0.60 ppm) and Mdha7 (0.80 ppm) are large compared with the corresponding differences for the other residues ($\Delta\delta^{13}$C < 0.5 ppm), which support the conformational difference observed in this region of the peptides. Additionally, the observed amide resonances, H^N ($\Delta\delta$H^N = 0.24 ppm) and ^{15}N ($\Delta\delta^{15}$N $= -2.00$ ppm), in Glu6 also differ substantially between MCLR and MCRR.

The difference in temperature coefficient (Table 3) for Glu6 also indicates that the hydrogen bonds are weaker or absent in MCLR. In the calculated structures of MCLR no hydrogen bonds were found to Glu6-H^N, while in MCRR there were hydrogen bonds between this proton and the oxygens in the -COO$^-$ group of Masp3. In the complex between MCLR and PP-1, this carboxylate group is not involved in any intra molecular hydrogen bonding but observed to form hydrogen bonds with Arg96 and Tyr143 in the protein [23]. Accordingly, the observed lower toxicity of MCRR [15] may be related to the need for breaking these intramolecular bonds in MCRR before binding to the enzyme.

The temperature coefficients for the amino acids Glu6, Ala1 and Arg2/Leu2 are generally smaller in MCRR as compared to MCLR (Table 3). These findings are in accordance with the more compact saddle structure for MCRR, which will make these amide groups more shielded from the solvent. Another observed difference between MCRR and MCLR is the non-linear change of the temperature coefficient for Arg2 observed in MCRR. The change in solvent accessibility for this amide proton may be an indication that this amino acid can adopt other conformations at temperatures above 25°C.
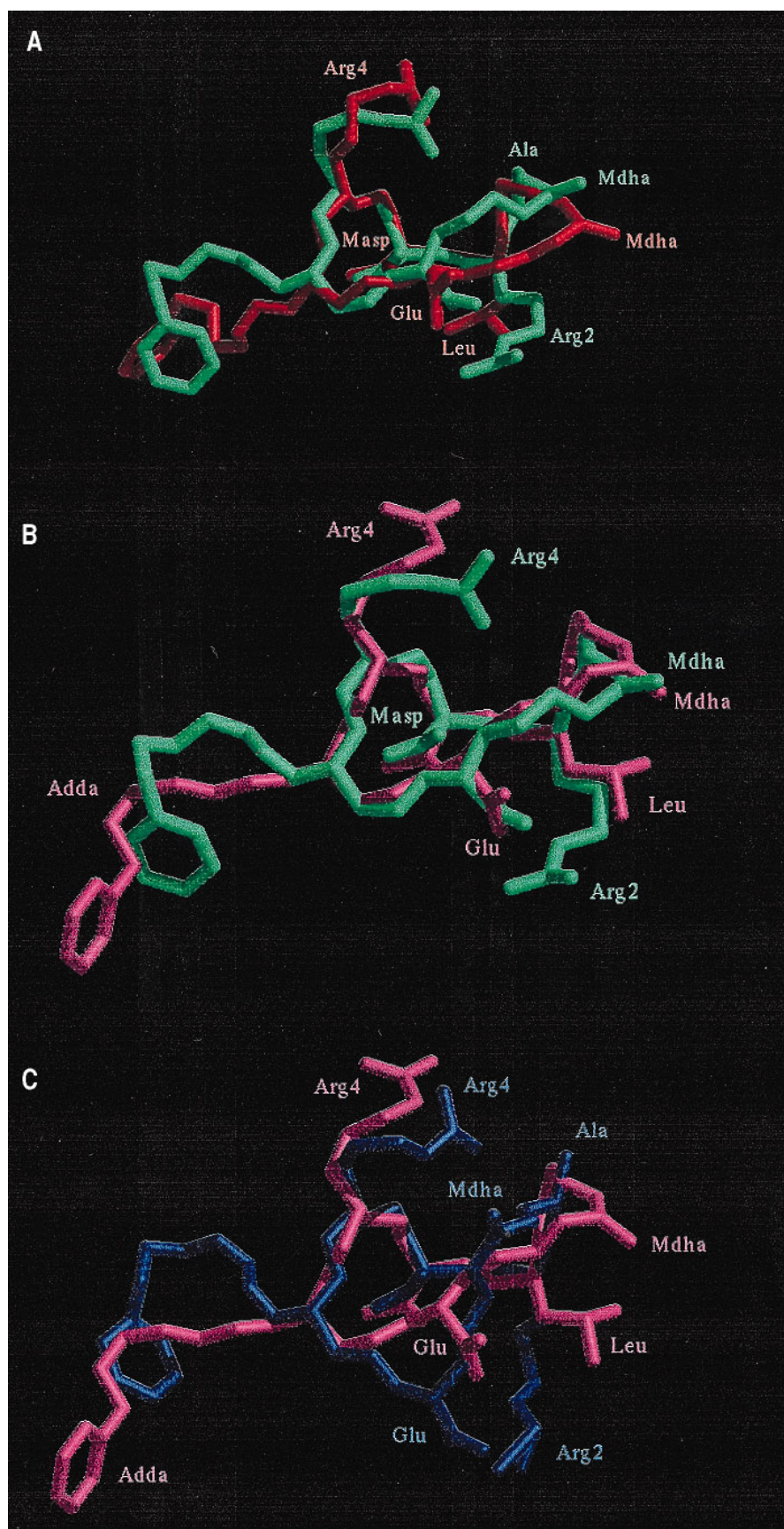
Trogen et al. (*Eur. J. Biochem. 258*)

Fig. 7. Superimposition of structures of MCRR with solution and crystal structures of MCLR. (A) Superimposition of the minimized free average structure (cryoprotective solvent) of microcystin-LR onto the minimized average structure of family A of microcystin-RR. The red structure and red labeled residues belong to microcystin-LR. (B) Superposition of the minimized average structure of family A (green) onto the bound crystal structure of microcystin-LR (magenta). (C) Comparison between the minimized average structure of family B (blue) and the bound crystal structure of microcystin-LR (magenta). The structures in all the panels were fitted to minimize the rmsd for the backbone atoms of residues 2−5.

The free average minimized solution structures of family A and family B of MCRR were compared with that of MCLR bound to PP-1 (Fig. 7B,C). The rmsds of the backbone atoms superimposed on each other was 0.56 pm (family A) and 1.37 pm (family B), respectively. The corresponding value for MCLR in the same solvent mixture was 79 pm. When the backbone segment of the Arg2-Masp3-Arg4-Adda5 atoms of MCRR (i.e. the segment with the largest differences excluded) was superimposed onto the corresponding atoms of bound crystal MCLR, the rmsd was 40 pm for family A and 44 pm for family B. The average free minimized solution structure of MCLR was also compared with the minimized structures of families A and B. The backbone atoms from the segment Arg2-Masp3-Arg4-Adda5 were superimposed onto each other. The rmsd between the structures were 37 pm (A) and 44 pm (B) respectively. These data clearly show the similarities in the backbone atoms of the residues from Arg2/Leu2 up to Adda5 between MCRR and MCLR. They also show that the largest differences can be found in the segment consisting of the residues Glu, Mdha, and Ala which is consistent with all the measured NMR parameters.

CONCLUSION

Our results indicate that the major part of microcystin-RR in solution essentially adopts a single backbone conformation, although two different conformations can be observed in the region of Glu6−Ala1. The results of the unrestrained MD calculations support the presence of two conformations. This condition is also reflected in the NMR data which are obtained as an average of values for exchanging conformers. The Adda side chain appears to adopt the same, well defined conformation in both families, but our data suggest that this is an artifact caused by the NOE constraints.

When the structures of microcystin-RR were compared with microcystin-LR, both in solution and in the protein-bound crystal structure, it was seen that the saddle-shape of the macrocyclic ring is more accentuated and compact in microcystin-RR. As a result, the hydrogen-bonding pattern in the two peptides are different as well as the position of the olefinic group in Mdha7. The observed differences between the calculated structures of the two peptides are confirmed by the chemical shifts of the backbone atoms and the observed temperature coefficients of the amide protons.

The crystal structure of the complex between MCLR and PP1 [23] shows that there are hydrophobic interaction between Leu2 in MCLR and a Tyr in protein phosphatase, which may be significant for the difference in toxicity between MCLR and MCRR. However, the structural differences of the macrocyclic ring and hydrogen bonding pattern of MCLR and MCRR observed in this work, may also contribute to the lower toxicity of microcystin-RR, since its structure has to undergo a conformational change to allow the formation of the tight complex observed between microcystin-LR and protein phosphatase. The relative importance of these contributions can only be assessed when the structure of the MCRR-PP1 complex is known.

REFERENCES

1. Fischer, E. H. & Brautigan, D. L. (1982) A phosphatase by any other name : from prosthetic group removing enzyme to phosphorylase phosphatase, *Trends Biochem. Sci. 7*, 3−4.

2. Honkanen, R. E., Zwiller, J., Daily, S. C., Khatra, B. S., Dukelow, M. & Boynton, A. L. (1991) Identfication, purification, and characterization of a novel serine/threonine protein phosphatase from bovine brain, *J Biol. Chem. 266*, 6614−6619.

3. MacKintosh, C. & MacKintosh, R. W. (1994) Inhibitors of protein kinases and phosphatases, *Trends Biochem. Sci. 19*, 444−448.

4. Cohen, P. (1989) The structure and regulation of protein phosphatases, *Annu. Rev. Biochem. 58*, 453−508.

5. Eriksson, J. E. & Golman, R. D. (1993) Protein phosphatase inhibitors alter cytoskeletal structure and cellular morphology, *Adv. in Protein Phosphatases 7*, 335−357.

6. Fischer, E. H., Charbonneau, H. & Tonks, N. K. (1991) Protein tyrosine Phosphatases : a diverse family of intracellular and transmembrane enzymes, *Science 253*, 401−406.

7. Nishiwaki-Matsushima, R., Ohta, T., Nishiwaki, S., Suganuma, M., Kohyama, K., Ishikawa, T., Carmichael, W. W. & Fujiki, H. (1992) Liver tumor promotion by the cyanobacterial cyclic peptide toxin microcystin-LR, *J. Cancer Res. Clin. Oncol. 118*, 420−424.

8. Matsushima, R., Yoshizawa, S., Watanabe, M. F., Harada, K., Furusawa, M., Carmichael, W. W. & Fujiki, H. (1990) In vitro and in vivo effects of protein phosphatase inhibitors, microcystins and nodularin, on mouse skin and fibroblasts, *Biochem. Biophys. Res. Commun. 171*, 867−874.

9. Honkanen, R. E., Zwiller, J., Moore, R. E., Daily, S. C., Khatra, B., Dukelow, M. & Boynton, A. L. (1990) Characterization of microcystin-LR, a potent inhibitor of type 1 and type 2A protein phosphatases, *J. Biol. Chem. 265*, 19401−19404.

10. MacKintosh, C., Beatlie, K. A., Klumpp, S., Cohen, P. & Codd, G. A. (1990) Cyanobacterial microcystin-LR is a potent and specific inhibitor of protein phosphatases 1and 2A from both mammals and higher plants, *FEBS Lett. 264*, 187−192.

11. Sivonen, K., Namikoshi, M., Evans, W. R., Carmichael, W. W., Sun, F., Rouhainen, L., Luukkainen, R. & Rinehart, K. L. (1992) Isolation and characteriazation of a variety of microcystins from seven strains of the cyanobacterial genus Anabena, *Appl. Environ. Microbiol. 58*, 2495−2500.

12. de Silva, E. D., Williams, D. E., Andersen, R. J., Klix, H., Holmes, C. F. B. & Allen, T. M. (1992) Motuporin, a potent protein phosphatase inhibitor isolated from the Papua New Guinea sponge Theonella swinhoei Gray, *Tetrahedron Lett. 33*, 1561−1564.

13. Carmichael, W. W. (1992) Cyanobacteria secondary metabolites − the cyanotoxins, *J. Appl. Bact. 72*, 445−459.

14. Toivola, D., Eriksson, J. E. & Brautigan, D. I. (1994) Identification of protein phosphatase 2A as the primary target for microcystin-LR in rat liver homogenates, *FEBS Lett. 344*, 175−180.

15. Rinehart, K. L., Namikoshi, M. & Choi, B. W. (1994) Structure and biosynthesis of toxins from blue-green algae (cyanobacteria), *J. Appl. Physiol. 6*, 159−176.

16. Sivonen, K., Kononen, K. L., Carmichael, W. W., Dahlem, A. M., Rinehart, K. L., Kiviranta, J. & Niemelä, S. I. (1989) Occurrence of the hepatotoxic cyanobacterium *Nodularia spumigena* in the Baltic Sea and structure of the toxin, *Appl. Environ. Microbiol. 55*, 1990−1995.

17. Namikoshi, M., Rinehart, K. L., Sakai, R., Slotts, R. R., Dahlem, A. M. & Beasley, V. R. (1992) Identification of 12 hepatotoxins from a Homer Lake bloom of the cyanobacteria *Microcystis aeruginosa*, *Microcystis viridis*, and *Microcystis wesenbergii*: nine new microcystins, *J. Org. Chem. 57*, 866−872.

18. Rudolpf-Böhner, S., Mierke, D. F. & Moroder, L. (1994) Molecular structure of the cyanobacterial tumor-promoting microcystins, *FEBS Lett. 349*, 319−323.

19. Bagu, J. R., Sykes, B. D., Craig, M. M. & Holmes, C. F. B. (1997) A molecular basis for different interactions of marine toxins with protein phosphatase-1, *J. Biol. Chem. 272*, 5087−5097.

20. Mierke, D. F., Rudolph-Böhner, S., Müller, G. & Moroder, L. (1995) Structure of two microcystins : refinement with nuclear Overhauser effects and ensemble calculations, *Biopolymers 36*, 811−828.

21. Trogen, G.-B., Annila, A., Eriksson, J., Kontteli, M., Meriluoto, J., Sethson, I., Zdunek, J. & Edlund, U. (1996) Conformational studies of microcystin-LR using NMR spectroscopy and molecular dynamics calculations, *Biochemistry 35*, 3197−3205.

22. Annila, A., Lehtimäki, J., Mattila, K., Friksson, J. E., Sivonen, K, Rantala, T. T. & Drakenberg, Y. (1996) Solution structure of nodularin, *J. Biol. Chem. 271*, 16 695−16 702.

23. Goldberg, J., Huang, H., Kwon, Y., Greengard, P., Nairn, A. G. & Kuriyan, J. (1995) Three-dimensional structure of the catalyitc subunit of protein serine/threonine phosphatase-1, *Nature 376*, 745−753.

24. MacKintosh, R. W., Dalby, K. N., Campbell, D. G., Cohen, P. T. W., Cohen, P. & MacKintosh, C. (1995) The cyanobacterial toxin microcystin binds covalently to cysteine-273 on protein phosphatase 1, *FEBS Lett. 371*, 236−240.

25. Taylor, C. & Quinn, R. J. (1996) Synthesis of cyclic peptides modelled on the microcystin and nodularin rings, *Bioorg. Med. Chem. Lett. 6*, 2107−2112.

26. Taylor, C. & Quinn, R. J. (1996) Inhibition of protein phosphatase 2A by cyclic peptides modelled on the microcystin ring, *Bioorg. Med. Chem. Lett. 6*, 2113−2116.

27. Shichman, S. A. & Amey, R. L. (1971) Viscosity and local liquid structure in dimethyl sulfoxide-water mixtures, *J. Phys. Chem. 75*, 98−102.

28. Saulitis, J., Mierke, D. F., Byk, G., Gilon, C. & Kessler, H. (1992) Conformation of cyclic analogues of substance P: NMR and molecular dynamics in dimethyl sulfoxide, *J. Am. Chem. Soc. 114*, 4818−4827.

29. Rance, M., Sørensen, O. W., Bodenhausen, G., Wagner, G., Ernst, R. R. & Wüthrich, K. (1983) Improved spectral resolution in COSY ^{1}H-NMR spectra of proteins via double quantum filtering, *Biochem. Biophys. Res. Commun. 117*, 479−485.

30. Braunschweiler, L. & Ernst, R. R. (1983) Coherence tmsfer by isotropic mixing: application to proton correlation spectroscopy, *J. Magn. Reson. 53*, 521−528.

31. Redfield, A. G. & Kunz, S. D. (1975) Quadrature fourier NMR detection: simple multiplex for dual detection and discussion, *J. Magn. Reson. 19*, 250−254.

32. Marion, D. & Wüthrich, K. (1983) Application of phase sensitive two-dimensional correlated spectroscopy (COSY) for measurements of ^{1}H-^{1}H spin-spin coupling constants in proteins, *Biochem. Biophys. Res. Commun. 113*, 967−974.

33. Jeener, J., Meier, B. H., Bachmann, P. & Ernst, R. R. (1979) Investigation of exchange processes by two-dimensional NMR spectroscopy, *J. Chem. Phys. 71*, 4546−4553.

34. Marion, D., Ikura, M., Tschudin, R. & Bax, A. (1989) Rapid recording of 2D NMR spectra without phase cycling. Application to the study of hydrogen exchange in proteins, *J. Magn. Reson. 85*, 393−399.

35. Brown, S. C., Weber, P. L. & Mueller, L. (1988) Toward complete ^{1}H NMR spectra in proteins, *J. Magn. Reson. 77*, 166−169.

36. Kay, L. E. (1993) Pulsed-field gradient-enhanced three-dimensional NMR experiment for correlating $^{13}C\alpha/\beta$, $^{13}C'$, and $^1H\alpha$ chemical shifts in uniformly ^{13}C-labeled proteins dissolved in H$_2$O, *J. Am. Chem. Soc. 115*, 2055−2057.

37. Wishart, D. S., Bigam, C. G., Yao, J., Ablidgaard, F., Dyson, H. J., Oldfield, E., Markley, J. L. & Sykes, B. D. (1995) ^{1}H, ^{13}C and ^{15}N chemical shift referencing in biomolecular NMR, *J. Biomol. NMR 6*, 135−140.

38. Borgias, B. A. & James, T. L. (1989) Two-dimensional nuclear Overhauser effect: complete relaxation matrix analysis, *Methods Enzymol. 176*, 169−183.

39. Borgias, B. A. & James, T. L. (1990) MARDIGRAS − A procedure for matrix analysis of relaxation for discerning geometry of an aqueous structure, *J. Magn. Reson. 87*, 475−487.

40. Suzuki, E., Pattabiraman, N., Zon, G. & James, T. L. (1986) Solution structure of [d(A-T)$_5$]$_2$ via complete relaxation matrix analysis of two-dimensional nuclear Overhauser effect spectra and molecular mechanics calculations: evidence for a hydration tunnel, *Biochemistry 25*, 6854−6865.

41. Widmer, H. & Wüthrich, K. (1986) Simulation of two-dimensional NMR experiments using numerical density matrix calculations, *J. Magn. Reson. 70*, 270−279.

42. Widmer, H. & Wüthrich, K. (1987) Simulated two-dimensional NMR cross-peak fine structures for ^{1}H spin systems in polypeptides and polydeoxynucleotides, *J. Magn. Reson. 74*, 316−336.

43. Bystrov, V. F. (1976) Spin-spin coupling and the conformation states of peptide systems, *Progr. Nuclear Magn. Reson. Spectr. 10*, 41−81.

44. Brünger, A. T. (1992) *XPLOR manual* (version 3.1) Yale University Press, New Haven, CT.

45. Brooks, B. R., Bruccoleri, R. E., Olafson, B. D., States, D. J., Swaminathan, S. & Karplus, M. (1983) CHARMM: a program for macromolecular energy, minimization, and dynamics calculations, *J. Comput. Chem. 4*, 187−217.

46. Edmonson, S., Khan, N., Shriver, J., Zdunek, J. & Gräslund, A. (1991) The solution structure of motilin from NMR distance constraints, distance geometry, molecular dynamics, and an iterative full relaxation matrix refinement, *Biochemistry 30*, 11 271−11 279.

47. Gochin, M. & James, T. L. (1990) Solution structure studies of d(AC)$_4$ · d(GT)$_4$ via restrained molecular dynamics simulations with NMR constraints derived from two-dimensional NOE and double-quantum-filtered COSY experiments, *Biochemistry 29*, 11 172−11 180.

48. Thomas, P. D., Basus, V. J. & James, T. L. (1991) Protein solution structure determination using distances from two-dimensional nuclear Overhauser effect experiments: effect of approximations on the accuracy of derived structures, *Proc. Natl Acad. Sci. USA 88*, 1237−1241.

49. Wüthrich, K. (1986) *NMR of proteins and nucleic acids*, John Wiley & Sons, Inc., New York.

50. Harada, K.-I., Ogawa, K., Matsuura, K., Murata, H., Suzuki, M., Watanabe, M. F., Itzeno, Y. & Nakayama, N. (1990) Structural determination of geometrical isomers of microcystins LR and RR from cyanobacteria by two-dimensional NMR spectroscopic techniques, *Chem. Res. Toxicol. 3*, 473−481.

51. Pardi, A., Billeter, M. & Wüthrich, K. (1984) Calibration of the angular dependence of the amide proton-C$^\alpha$ proton coupling constants, $^3J_{\mathrm{HN}\alpha}$, in a globular protein. Use of $^3J_{\mathrm{HN}\alpha}$ for identification of helical secondary structure, *J. Mol. Biol. 180*, 741−751.

52. Ohnishi, M. & Urry, D. W. (1969) Temperature dependence of amide proton chemical shifts: the secondary structure of gramicidin S and valinomycin, *Biochem. Biophys. Res. Commun. 36*, 194−202.

53. Mierke, D. F., Geyer, A. & Kessler, H. (1994) Coupling constants and hydrogen bonds as experimental restraints in a distance geometry refinement protocoll, *Int. J. Peptide Protein Res. 44*, 325−331.

54. Williamson, M. P. & Waltho, J. P. (1992) Peptide Structure from NMR, *Chem. Soc. Rev. 21*, 227−236.

55. Oldfield, E. (1995) Chemical shifts and three-dimensional protein structures, *J. Biomol. NMR 5*, 217−225.